NANO · MICRO small
www.small-journal.com

Correlating Rate-Dependent Transition Metal Dissolution between Structure Degradation in Li-Rich Layered Oxides

Bo Cao, Tianyi Li, Wenguang Zhao, Liang Yin, Hongbin Cao, Dong Chen, Luxi Li, Feng Pan,* and Mingjian Zhang**

Understanding the mechanism of the rate-dependent electrochemical performance degradation in cathodes is crucial to developing fast charging/discharging cathodes for Li-ion batteries. Here, taking Li-rich layered oxide $Li_{1.2}Ni_{0.13}Co_{0.13}Mn_{0.54}O_2$ as the model cathode, the mechanisms of performance degradation at low and high rates are comparatively investigated from two aspects, the transition metal (TM) dissolution and the structure change. Quantitative analyses combining spatial-resolved synchrotron X-ray fluorescence (XRF) imaging, synchrotron X–ray diffraction (XRD) and transmission electron microscopy (TEM) techniques reveal that low-rate cycling leads to gradient TM dissolution and severe bulk structure degradation within the individual secondary particles, and especially the latter causes lots of microcracks within secondary particles, and becomes the main reason for the fast capacity and voltage decay. In contrast, high-rate cycling leads to more TM dissolution than low-rate cycling, which concentrates at the particle surface and directly induces the more severe surface structure degradation to the electrochemically inactive rock-salt phase, eventually causing a faster capacity and voltage decay than low-rate cycling. These findings highlight the protection of the surface structure for developing fast charging/discharging cathodes for Li-ion batteries.

1. Introduction

Fast charging/discharging capability has become a pressing demand for Li-ion batteries especially in electric vehicles.[1] It loads great pressure for developing cathodes with excellent rate performance. Many strategies, like conductive additives, elemental lattice doping, nanometerization, core-shell heterostructure, etc., have been developed to enhance the rate performance of cathode materials. Carbon nanotubes, Pt/Ag additives etc., were introduced to prepare electrodes with the better conductive network for higher rate capability.[2] Multiple elemental doping approaches, including Mn/La co-doping, Al/Ti co-doping, etc., were reported to improve the Li^+ diffusivity of $LiCoO_2$, thus delivering a better rate performance.[3] Nanosized $LiCoO_2$ with various morphologies, including "desert rose", parallelly arranged nanoplatelets, 3D nanosheets, etc., have been synthesized, exhibiting the high rate capability due to the shortened Li^+ diffusion pathway.[4] Similarly, Chou et al. synthesized few-layered nanosheets of $LiCoO_2$, $LiMn_2O_4$, and $LiFePO_4$, which all present superior rate capability.[5] In addition, the core-shell structured $LiNi_{0.5}Mn_{1.5}O_4$ with $LiCoO_2$ shell delivers high-rate performance due to the better ionic conductivity of $LiCoO_2$.[6] These researches mainly focus on increasing the capacity at high rates, while ignoring the cycling stability at high rates, which is also critical for the practical application of high-rate cathodes. To solve the concern, it is essential and preferential to figure out the mechanism of the performance degradation at high rates, which could guide the modification strategies.

TM dissolution in cathodes is one of the important factors affecting electrochemical performance during cycling. The current main-stream cathodes, $LiCoO_2$, $LiMn_2O_4$, $LiFePO_4$, $LiTMO_2$ (TM = Ni/Co/Mn), Li-rich layered oxides, and etc., all contain transition metals (TMs), Co, Ni, Mn, Fe, etc.[7] During the charge/discharge, these TM cations not only act as the pool of electron extraction/insertion via various redox couples, like Co^{3+}/Co^{4+}, Ni^{3+}/Ni^{4+}, Mn^{3+}/Mn^{4+}, and Fe^{2+}/Fe^{3+}, more importantly, serve as the framework ions in the highly-delithiated cathodes under the deep charge state.[7a] Thus, the changes in the TM composition would greatly affect the electrochemical performance of cathodes, including the reversible capacity and structural stability. Tarascon et al. reported Co dissolution in $LiCoO_2$ could induce the capacity decrease in 1996.[7g] In 1981, Hunter et al. observed serious Mn dissolution in $LiMn_2O_4$,[8] which came

B. Cao, W. Zhao, H. Cao, D. Chen, F. Pan
School of Advanced Materials
Peking University
Shenzhen Graduate School
Shenzhen 518055, People's Republic of China
E-mail: panfeng@pkusz.edu.cn
T. Li, L. Yin, L. Li
X-ray Science Division
Advanced Photon Source
Argonne National Laboratory
Lemont, IL 60439, USA
E-mail: luxili@anl.gov
M. Zhang
School of Science and Engineering
The Chinese University of Hong Kong
Shenzhen 518172, China
E-mail: zhangmingjian@cuhk.edu.cn
The ORCID identification number(s) for the author(s) of this article can be found under https://doi.org/10.1002/smll.202301834

DOI: 10.1002/smll.202301834

from the side reactions between surficial Mn^{3+} with trace HF in the electrolyte.[9] It led to the formation of MnF_2 and MnO-like species on the surface,[9a,9c] and induced the growing up of the microcracks, which sped up the side reactions with the electrolyte in return.[10] These researches are almost conducted at low rates, while the influences of increasing the rate on the TM dissolution are unknown hitherto.

The irreversible bulk/local structure deterioration in cathodes is another important factor to induce the performance degradation. Recently, Pan et al. adopted three-dimensional electron diffraction technique to reveal that, the TM layers became bent with cycling, hindering Li^+ transportation and resulting in a fast capacity decrease at high voltages.[11] Liu et al. systemically studied the structure changes of spinel $LiMn_2O_4$ during cycling, and found that, the irreversible cubic-tetragonal phase transformation induced by serious Jahn-Teller distortion of $Mn^{3+}O_6$ octahedra was the origin of the fast capacity fading.[12] In high-Ni cathodes, a series of phase transitions of H1-H2-M1-H3 would accumulate strain within and among the primary particles, which induces the microcracks, and eventually leading to fast performance degradation.[13] Therefore, the structure changes with cycling must be examined to study the performance degradation mechanism in cathodes.

In this work, we comparatively investigated the mechanisms of performance degradation of Li-rich Mn-based layered oxide $Li_{1.2}Ni_{0.13}Co_{0.13}Mn_{0.54}O_2$ (LR114) at low and high rates from two aspects, the transition metal (TM) dissolution and the change of bulk/local structure. Spatially-resolved synchrotron-based X-ray Fluorescence (XRF) imaging technique was adopted to quantitatively investigate TM dissolution with cycling. Synchrotron radiation X-ray diffraction (XRD) combined with Rietveld refinements was used to quantify the bulk structure degradation with cycling. The local structure change within the secondary particle was examined by high-resolution TEM. Combining these advanced characterizations, the rate-dependent electrochemical degradation mechanisms were clearly revealed.

2. Results and discussion

2.1. Rate-Dependent Electrochemical Degradation

To study the electrochemical degradation at different rates, all LR114 cathodes with the typical layered structure (**Figure 1**a; Figure S1, Supporting Information) were activated in the initial three cycles at 0.1 C (1 C = 250 mA g^{-1}) and then cycled at different rates. Figure 1b–d show the charge/discharge profiles at the selected cycles under 0.2, 1, and 2 C. The initial discharge capacities at 1 and 2 C are 275 and 262 mA h g^{-1}, respectively, ≈92% and 88% of that at 0.2 C (299 mA h g^{-1}). The discharge capacity and voltage all keep degenerating with cycling at different rates, consistent with the previous reports.[14] To directly compare the degradation speeds of electrochemical performance at different rates, the capacity retentions and the average voltages were plotted versus the cycle number in Figure 1e,f, respectively. The capacity retentions decrease fast in the initial 10 cycles, and gradually decrease to 82%, 77%, and 73% after 200 cycles at 0.2, 1, and 2 C, respectively. The average voltages show similar curves, and the voltage decays are 0.4064, 0.4669, and 0.4939 V after 200 cycles, respectively. Overall, the degradation speeds of the capacity retention and average voltage become faster with the increasing rate, and the cycling stability becomes much poorer at high rates than at low rates.

2.2. Quantifying TM Dissolution

To quantify the TM dissolution upon cycling, synchrotron-based spatial-resolved XRF as a powerful tool to monitor the elemental distribution at the micrometer scale, was employed here. **Figure 2**a presents the Mn, Ni, and Co distribution maps on the Li anodes after different cycle numbers at 1 C. The signals gradually become intensive with the cycle number, indicating that, the amounts of Mn/Ni/Co dissolution increase with the cycle number. Moreover, the element-enrich areas (light contrast) and element-poor areas (dark contrast) for Mn, Ni, and Co are consistent on the Li anodes, showing the spatial correlation of TM distribution. According to the contrast difference, the area can be divided into the middle region and the edge region by the dashed circles in Figure 2a. In the first 20 cycles, the middle regions have less TM amounts than the edge regions, indicating the preferential TM deposition at the edge regions. Then Mn/Ni/Co quickly accumulate in the middle region with the cycle number. Similar phenomena are observed in the element maps at 0.2 and 2 C (Figure S2 and S3, Supporting Information), consistent with the previous report.[15] It may be associated with the non-uniform surface roughness and pressure distribution (see the detailed analysis below Figure S3, Supporting Information). In addition, the Mn/Ni/Co concentration statistics profiles (Figure S4) were extracted from the corresponding element maps in Figure 2a (Supporting Information). A narrow peak appears at ≈0.2 μg cm^{-2} after the 1st cycle, corresponding to the preferential and uniform TM deposition outside of the indentation regions. Upon further cycling, its intensity continuously decays with the cycle number, while a new broad peak gradually appears and intensifies at ≈0.6 μg cm^{-2}, mainly ascribed to the TM deposition in the indentation regions. The gradual increase in the peak broadness indicates the non-uniform TM deposition with cycling. A similar phenomenon is observed in the Mn/Ni/Co concentration statistics profiles at 2 C (Figure S5, Supporting Information).

The total amounts of Mn/Ni/Co dissolution were summarized in Figure 2b,d; Figure S6 (Supporting Information). As shown in Figure 2b (Supporting Information), TM dissolution maintains at a low level in the first 10 cycles, and then fast increases with the cycle number. It demonstrates that, TM dissolution has no direct relationship with the fast capacity decay in the first 10 cycles (Figure 1e). Since Co dissolution is the smallest of three kinds of TM cations, we deduce the Ni/Co and Mn/Co molar ratios in Figure 2c. Mn/Co ratio keeps at ≈2 in the initial 10 cycles, then gradually increases with cycling and approaches 3.5 after 200 cycles. The value is still smaller than the stoichiometric ratio of 4 in LR114, indicating the slower dissolution rate of Mn than that of Co. Ni/Co ratio maintains at 1 (the stoichiometric ratio in LR114) in the first 20 cycles and gradually increases with the cycle number. It indicates that, the Mn/Ni/Co dissolution speeds are not synchronous. The rate of Mn dissolution is slower than that of Ni and Co dissolution initially, and then gradually accelerates with cycling, while Ni dissolution rate is similar to that of Co initially, and the accelerated speed of Ni dissolution is larger than

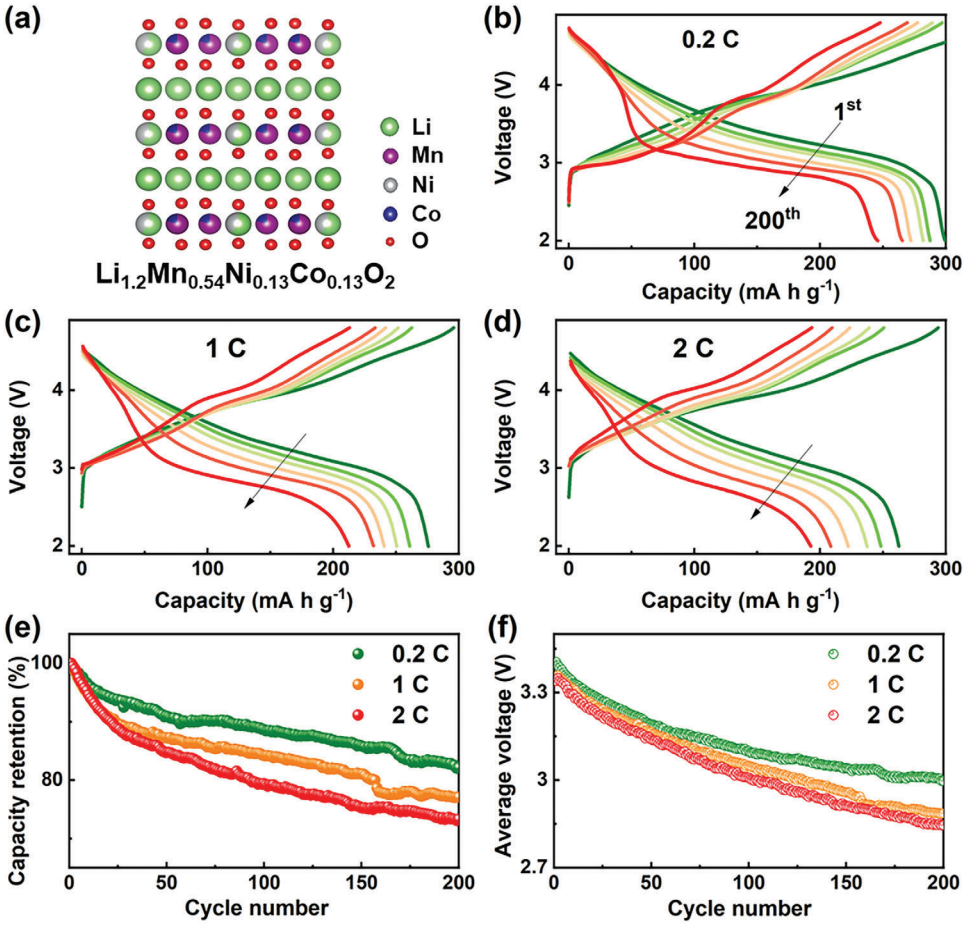

Figure 1. Electrochemical degradation of Li-rich layered oxide at different rates. a) The layered structure of the model compound LR114. The 1st, 10th, 20th, 50th, 100th and 200th charge/discharge profiles of LR114 cathodes at 0.2 (b), 1 (c), and 2 C (d). The plot of the capacity retention as a function of the cycle number at different rates (e). The plot of the average voltage as a function of the cycle number at different rates (f).

that of Co dissolution after 10–20 cycles. Similar phenomena are observed at other cycling rates (Figure 2d; Figure S7, Supporting Information). In addition, the total amounts of TM dissolution increase with the cycling rate. Mn/Co ratios at different rates are summarized in Figure 2e. It is clear that the ratios all change little in the first 20 cycles, then increase with the cycle number. The increasing slope becomes smaller with the rate, indicating that, the larger current rate would suppress the disproportion between Mn and Co dissolution.

Based on the quantitative analysis above, we can estimate the total amounts of TM dissolution after 200 cycles as 3.257, 3.962, 5.544 μg per cathode at 0.2, 1, and 2 C (see the dissolved Mn/Ni/Co amounts in Table S2, Supporting Information), respectively, if ignoring the small amounts of TM dissolved in the electrolyte (Figure S8, Supporting Information). They took about 0.61, 0.75, and 1.05 wt.% of TM content in the pristine cathode, respectively. The results are consistent with the previous report.[16] Such tiny elemental component changes could not explain the significant capacity and voltage decay above. Therefore, there is no direct relationship between TM dissolution and performance fade, and the performance fade may be directly related to the structure changes partially induced by TM dissolution.

2.3. Bulk Structure Changes

Synchrotron XRD was performed on the corresponding cathodes to examine the bulk structure changes upon cycling at different rates. The XRD patterns and the Rietveld refinement results were shown in Figure S9 and S10 (Supporting Information), and the detailed lattice parameters were deposited in Table S1 (Supporting Information) and plotted in **Figure 3**. As shown in Figure 3a–c, the changes of lattice parameters *a* and *c* show a similar trend at different rates. They change little in the initial 20 cycles, demonstrating good structural stability in the first 20 cycles. It indicates that, the fast capacity decrease in the first 20 cycles (Figure 1a) is not due to the bulk structure degradation. With further cycling, *a* increases with the cycle number while *c* decreases with the cycle number. It may be related to the continuous TM/O loss and the aggravated structural degradation from layered to spinel even to rock-salt phase with cycling.[13b,17] The variation values Δa and Δc after 200 cycles decrease with the increasing rate. It indicates that, the larger rate leads to the smaller changes in lattice parameters. Moreover, c/a ratio, as the common factor to evaluate the cationic ordering in the layered structure,[18] was deduced in Figure 3d. The ratios at different rates all exhibit the

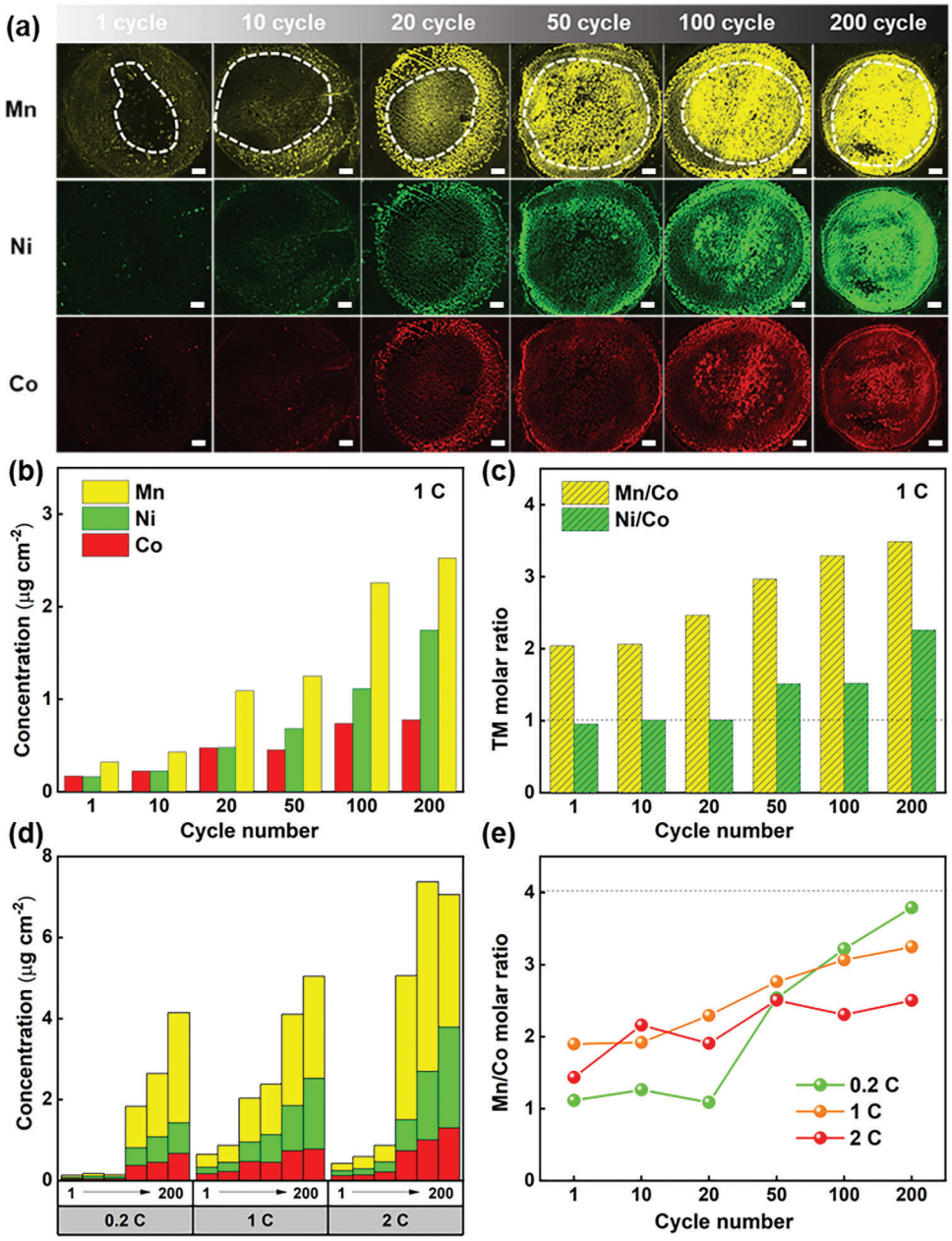

Figure 2. Quantify TM dissolution upon cycling. a) The Mn, Ni, and Co XRF coloring images of Li anodes at 1 C. The scale bars are 1 mm. The signal intensities were unified for each element for convenient comparison. b) The average concentrations of Mn, Ni, and Co on Li anodes with the cycle number at 1 C. c) The Mn/Co and Ni/Co molar ratios with the cycle number at 1 C. d) The average concentrations of Mn, Ni, and Co on Li anodes with the cycle number at different rates. e) The Mn/Co molar ratio with the cycle number at different rates.

decreasing trend with the cycle number, hinting the aggregated cationic disordering with cycling. In addition, the drop is much reduced with the increasing rate, consistent with the changing trend in the variations of lattice parameters. They both confirm that, the bulk structure degradation becomes slower with the increasing rate.

The impacts of the rate on the bulk structure changes can be illustrated in Figure 3e. Lattice parameter *a* increases while *c* decreases with cycling, and the cationic ordering decreases with cycling. With the increase of the current rate, the variations Δa and Δc decrease, while the variation of ordering degree ($\Delta ordering$) would be also suppressed. It is reasonable that, the high-rate cycling leads to much shadow charge/discharge, thus affecting the bulk structure less than the low-rate cycling.

2.4. Morphology and Local Structure Changes

The change in particle morphology was examined on the cross-section samples of the secondary particles prepared by the

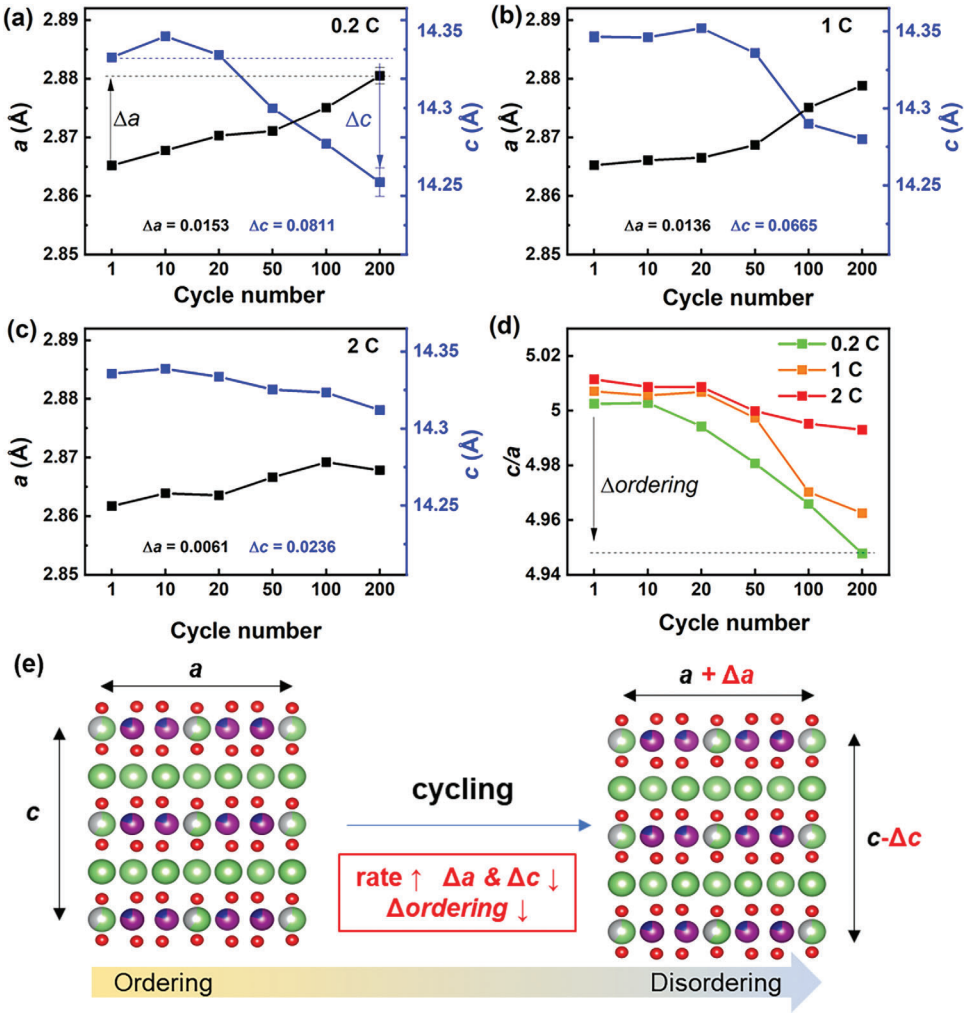

Figure 3. Bulk structure changes upon cycling at different rates. The changes of lattice parameters *a* and *c* with the cycle number at 0.2 (a), 1 (b), and 2 C (c). d) The *c*/*a* ratio with the cycle number at different rates. e) Schematic illustration to show the structure changes with cycling and the influences of the rate on the structure changes.

focused ion beam (FIB) technique. As shown in **Figure 4**a,d, the particle cycling at 0.2 C after 200 cycles exhibits lots of microcracks, while the particle cycling at 2 C still maintains the well mechanistic integrity. Similar phenomena can be observed in scanning electron microscopy (SEM) images of the selected-randomly particles after 200 cycles (Figure S11, Supporting Information). Depth-dependent X-ray photoelectron spectroscopy (XPS) (Figure S12, Supporting Information) was performed on the samples after 200 cycles at 0.2 and 2 C to check the microcracks on the surface chemistry. The lattice O signal was much weaker at 0.2 C than that at 2 C, and also the Mn and Co signals were observed after the longer etching time at 0.2 C than that at 2 C. These phenomena demonstrate more surface side reactions with low-rate cycling, which can be ascribed to the formation of lots of microcracks, which expose more surface area to the electrolyte.

To further check the local structure changes, we chose the near-surface region (marked by solid rectangles) and the inner region (marked by dashed rectangles) to collect high-resolution transmission electron microscopy (HRTEM) images. In Figure 4b, HRTEM image of the surface region in the low-rate cycling particle exhibits mixed phases compositing with much rock-salt phase, and small portions of layered and spinel phase, as demonstrated by the corresponding FFT map. The inner region of the low-rate-cycling particle is almost fully transformed to the spinel phase (Figure 4c). It indicates that, the whole secondary particle experienced serious structure degradation from surface to bulk after low-rate cycling, which should be responsible for the formation of microcracks. In comparison, the surface region of the high-rate-cycling particle completely transformed to the rock-salt phase (Figure 4e), while the inner region still maintains the layered structure (Figure 4f). It indicates that, the structure degradation mainly concentrates on the surface region after high-rate cycling, and the bulk structure is damaged little, which is consistent with the XRD results above. In brief, low-rate cycling leads to medium-degree structure degradation and thus the resulted microcracks throughout the secondary particle, while high-rate cycling leads to the more severe structure degradation in the rock salt phase mainly at the near-surface region.

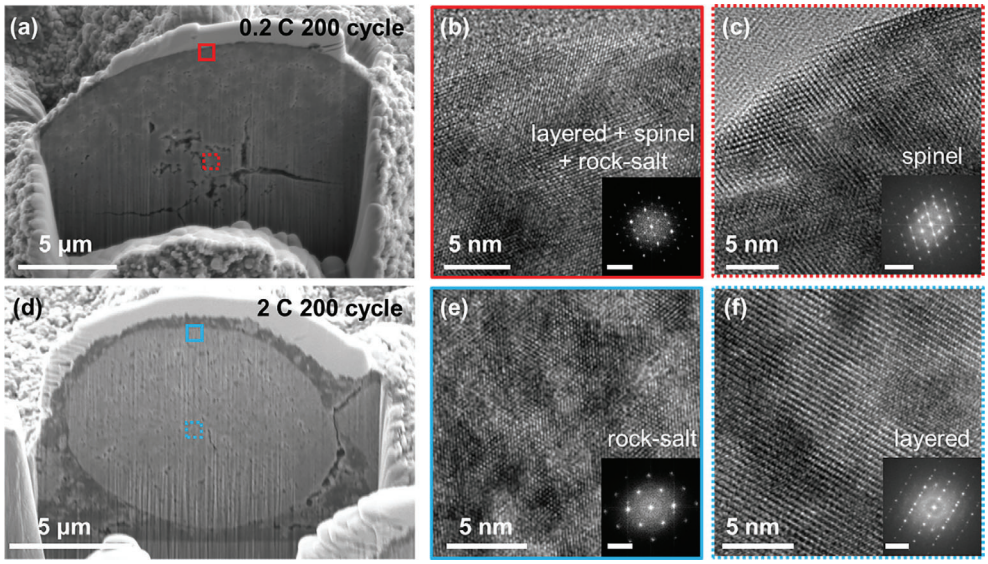

Figure 4. Local structure changes after cycling at different rates. a) SEM image of the cross-section sample of LR114 after 200 cycles at 0.2 C, prepared by FIB. HRTEM images and the corresponding FFT maps at the surface region (b) and the inner region (c) of the secondary particle in (a). d) SEM image of the cross-section sample of LR114 after 200 cycles at 2 C, prepared by FIB. HRTEM images and the corresponding FFT maps at the surface region (e) and the inner region (f) of the secondary particle in (d). The scalebars in the FFT maps are 5 1/nm.

2.5. Electrochemical Degradation Mechanism

Combining TM dissolution and structural changes together, we can deduce that, the electrochemical degradation mechanisms of Li-rich layered oxides vary with the rate. As shown in **Figure 5**, when cycling at low rates, TM cations gradually dissolve out from the bulk of the cathodes due to the deep charge/discharge, forming a full concentration gradient throughout the whole secondary particle. It brings with the severe and gradient structure degradation within the whole particle, including the structural transformation to spinel phase in the bulk and the further structure transformation to mixed phases with the main component rock-salt at the surface, inducing the strain accumulation and eventually the formation of lots of micro-cracks. Therefore, the electrochemical degradation at low rates can be mainly ascribed to the degradation of bulk structure and the destruction of particle mechanistic integrity. When cycling at high rates, more TM cations dissolve out than the low-rate cycling, and mainly concentrate at the near-surface region of the secondary particles, which results into the more severe deterioration of surface structure, especially the formation of the electrochemically-inactive rock-salt phase. The resulted surface rock salt phase greatly hinders the Li^+/electron transportation at the cathode/electrolyte interface, inducing a quicker decay of the capacity and average voltage than the low-rate cycling. In this high-rate case, the surface structure degradation brings with more serious influences on the electrochemical performance than the bulk structure degradation.

Moreover, the relationship between TM dissolution and structure change can be discussed based on the above quantitative analyses. Since TM dissolution only takes 0.61 wt.% of the TM content in the pristine cathode after low-rate cycling, moreover distributes gradient within the whole secondary particle. It is reasonable to deduce that, such tiny TM dissolution should have a relatively weak relationship with the severe structure degradation, which may be directly related to the accumulated strain and the continuous lattice O loss upon cycling.[17,19] Thus, the performance degradation at low rates may be mainly ascribed to the severe structure degradation not TM dissolution. Differently, high-rate cycling brings more TM dissolution, which concentrates at the surface region locally. Such local concentrated TM dissolution may become the direct inducement for the more severe surface structure degradation. Therefore, the much faster performance decay at high rates has a stronger relationship with the surface TM dissolution and the induced surface structure degradation.

3. Conclusion

In summary, we employed advanced synchrotron XRF imaging, synchrotron XRD, FIB-SEM and HRTEM techniques, combined with the electrochemical long-term cycling tests, to systemically investigate the performance degradation mechanisms of Li-rich layered oxide cathodes at varied rates. Quantitative analyses of XRF imaging data reveal the inhomogeneous and non-synchronous Mn/Ni/Co dissolution with cycling, and more severe TM dissolution at high rates than at low rates. Rietveld refinements of XRD data indicate that high-rate cycling leads to less bulk structure degradation than low-rate cycling. Visual observations by SEM and HRTEM reveal that, low-rate cycling results in lots of microcracks and severe structure degradation throughout the secondary particles, while high-rate cycling results in more severe structure degradation into the rock-salt phase concentrated at the particle surface. Combining these results together, the rate-dependent performance degradation mechanisms are clearly unraveled. When cycling at low rates, the breaking of mechanistic integrity of secondary particles due to the gradient TM dissolution and the structure degradation leads to the decay

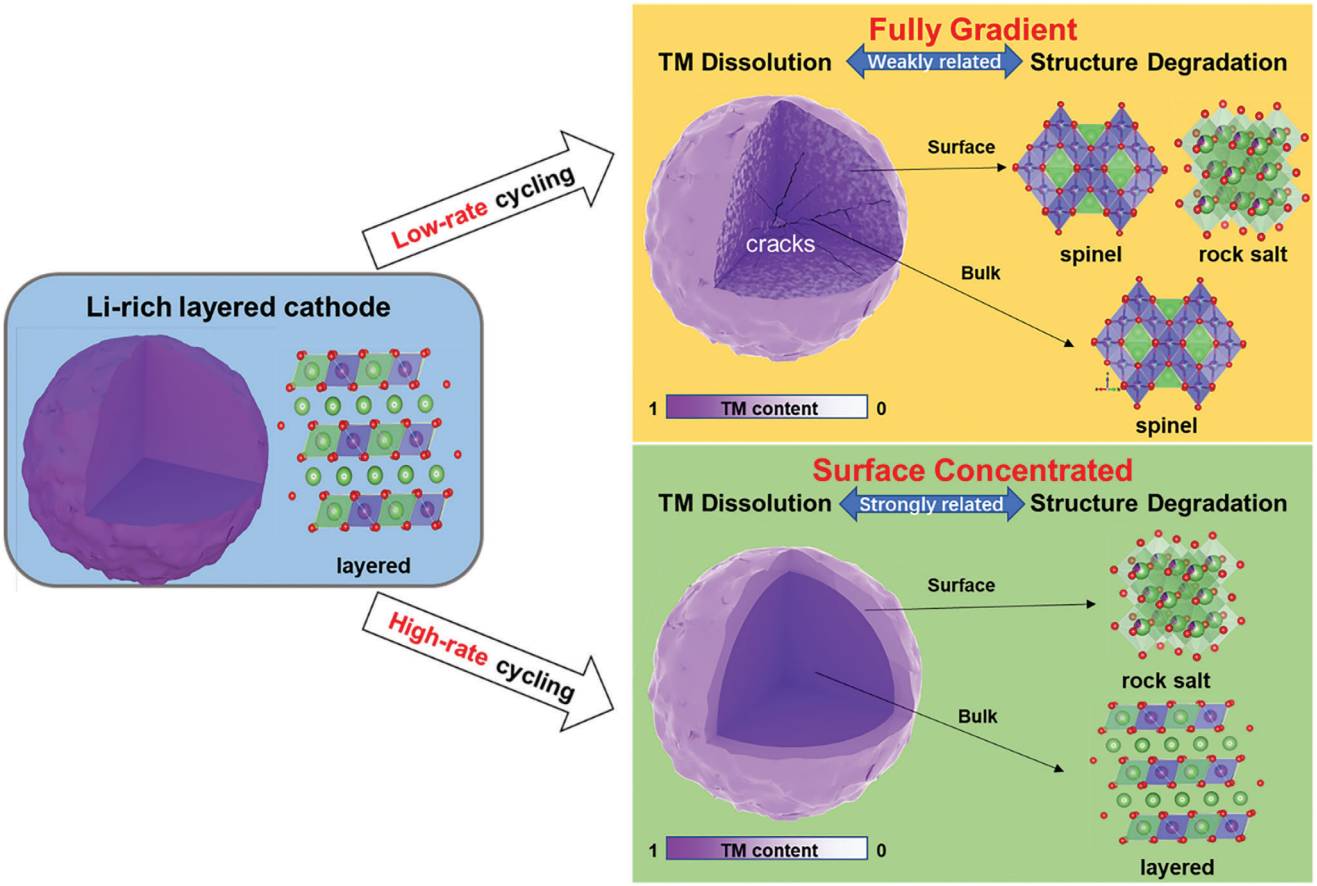

Figure 5. Schematic illustration of different electrochemical degradation mechanisms at low rate and high rates from two aspects, TM dissolution and structure degradation.

of capacity and average voltage. Differently, when cycling at high rates, the severe surface structure degradation due to the surface concentrated TM dissolution leads to a quicker performance decay than the low-rate cycling case. The findings emphasize the critical importance of stabilizing surface structure for achieving the cycling stability at high rates than at low rates, thus providing a guide to developing long-lifespan fast-charging/discharging cathodes through appropriate surface protection strategies.

4. Experimental Section

Electrochemical Tests: LR114 was purchased from Ningbo Fuli Battery Material Technology Co., Ltd. Electrochemical measurements were conducted with coin-type (CR2032) half cells. 10 wt.% of polyvinylidene fluoride (PVDF), 10 wt.% of acetylene black and 80 wt.% of LR114 sample were thoroughly mixed in N-methyl pyrrolidone (NMP). Then cast the slurry onto the aluminum foils, and dry at 105 °C in vacuum overnight to obtain the cathodes. The cathodes were cut into the discs with a diameter of 10 mm. The loading of LR114 per disc was ≈1 mg. The Li metal discs with a diameter of 18 mm were used as the anodes. The electrolyte was 1 M $LiPF_6$ solution in ethylene carbonate and dimethyl carbonate (EC/DMC v/v 1:1) with the additive of 5% fluoroethylene carbonate (FEC). The galvanostatic charge-discharge tests were performed using a NEWARE battery test system.

Synchrotron XRF Imaging: Ex situ XRF measurements were performed at the 8-BM-B beamline of the Advanced Photon Source (APS) at Argonne National Laboratory at room temperature. The sample was excited by 10 keV X-ray photons with a 30 µm beam size. Emitted XRF signals were then detected by an energy-dispersive detector while the sample was raster scanned with a step size of 25 µm and a dwell time of 100 ms. The minimum detection limits of synchrotron-based X-ray fluorescence were much higher than ppm levels sufficient to detect TM elements such as Mn, Ni, and Co. The 2D element concentrations were then calculated by MAPS43. Li metal anodes were disassembled from the corresponding cycled coin cells for mapping.

Synchrotron XRD: Synchrotron XRD (SXRD) measurements were performed at beamline 11-ID-C of the Advanced Photon Source (APS) at Argonne National Laboratory. Exhibiting high penetration and low absorption, synchrotron XRD precisely reflects bulk structure properties. A high-energy X-ray with a beam size of 0.2 mm × 0.2 mm and wavelength of 0.1173 Å was used to obtain 2D diffraction patterns in the transmission geometry. X-ray patterns were recorded with a Perkin-Elmer large-area detector placed at 1800 mm from the battery cells. For ex situ XRD sample preparation, powders from the cycled electrodes was scraped and sealed the samples with Kapton tape to avoid air exposure. The Rietveld refinements for ex situ XRD were performed with TOPAS software packages.

SEM, HRTEM, XPS and ICP-OES: The morphology of the individual secondary particles was characterized by scanning electron microscope (SEM, FEI Scios DualBeam) equipped with the focused ion beam (FIB). The local structures of the cross-section samples of the individual secondary particles were studied by high-resolution field-emission transmission electron microscopy (FETEM, JEOL-3200FS) at an accelerating voltage of 300 kV. The chemical states of the selected elements were investigated by X-ray photoelectron spectrometry (XPS) on a Thermo Scientific Escalab 250Xi spectrometer. The TM contents in the electrolyte were deter-

mined by inductively coupled plasma optical emission spectroscopy (ICP-OES, JY2000-2).

Supporting Information

Supporting Information is available from the Wiley Online Library or from the author.

Acknowledgements

This work was financially supported by the National Natural Science Foundation of China (52172175), the Shenzhen Science and Technology Research Grant (JCYJ20210324130812033, JCYJ20200109140416788), the Program from Guangdong Introducing Innovative and Entrepreneurial Teams (2019ZT08L101 and RCTDPT-2020-001), the Shenzhen Key Laboratory of Eco-materials and Renewable Energy (ZDSYS20200922160400001), the Basic and Applied Basic Research Foundation of Guangdong Province (2021B1515130002), the Chemistry and Chemical Engineering Guangdong Laboratory (1922018), the National Key R&D Program of China (2020YFB0704500), and the Major Science and Technology Infrastructure Project of Material Genome Big-science Facilities Platform supported by Municipal Development and Reform Commission of Shenzhen.

Conflict of Interest

The authors declare no conflict of interest.

Data Availability Statement

The data that support the findings of this study are available in the supplementary material of this article.

Keywords

Li-rich layered oxides, rate-dependence, structure degradation, transition metal dissolution, X-ray fluorescence imaging

Received: March 2, 2023
Revised: June 7, 2023
Published online:

[1] a) X. Jin, Y. H. Han, Z. F. Zhang, Y. W. Chen, J. M. Li, T. T. Yang, X. Q. Wang, W. X. Li, X. Han, Z. L. Wang, X. D. Liu, H. Jiao, X. X. Ke, M. L. Sui, R. G. Cao, G. Q. Zhang, Y. F. Tang, P. F. Yan, S. H. Jiao, *Adv. Mater.* **2022**, *34*, 2109356; b) R. Y. Tian, S. N. Park, P. J. King, G. Cunningham, J. Coelho, V. Nicolosi, J. N. Coleman, *Nat. Commun.* **2019**, *10*, 1933; c) G. L. Zhu, C. Z. Zhao, J. Q. Huang, C. X. He, J. Zhang, S. H. Chen, L. Xu, H. Yuan, Q. Zhang, *Small* **2019**, *15*, 1805389; d) S. S. Zhang, *Infomat* **2020**, *2*, 942; e) J. M. Zheng, M. H. Engelhard, D. H. Mei, S. H. Jiao, B. J. Polzin, J. G. Zhang, W. Xu, *Nat. Energy* **2017**, *2*, 17012; f) X. G. Yang, T. Liu, Y. Gao, S. H. Ge, Y. J. Leng, D. H. Wang, C. Y. Wang, *Joule* **2019**, *3*, 3002; g) Y. Yamada, K. Furukawa, K. Sodeyama, K. Kikuchi, M. Yaegashi, Y. Tateyama, A. Yamada, *J. Am. Chem. Soc.* **2014**, *136*, 5039.

[2] a) C. M. Ban, Z. Li, Z. C. Wu, M. J. Kirkham, L. Chen, Y. S. Jung, E. A. Payzant, Y. F. Yan, M. S. Whittingham, A. C. Dillon, *Adv. Energy Mater.* **2011**, *1*, 58; b) S. Luo, K. Wang, J. P. Wang, K. L. Jiang, Q. Q. Li, S. S. Fan, *Adv. Mater.* **2012**, *24*, 2294.

[3] a) T. Tian, T. W. Zhang, Y. C. Yin, Y. H. Tan, Y. H. Song, L. L. Lu, H. B. Yao, *Nano Lett.* **2020**, *20*, 677; b) L. L. Wang, J. Ma, C. Wang, X. R. Yu, R. Liu, F. Jiang, X. W. Sun, A. B. Du, X. H. Zhou, G. L. Cui, *Adv. Sci.* **2019**, *6*, 1900355.

[4] a) H. L. Chen, C. P. Grey, *Adv. Mater.* **2008**, *20*, 2206; b) S. Y. Zhou, T. Mei, J. P. Liu, X. B. Wang, Y. T. Qian, *ACS Appl. Mater. Interfaces* **2020**, *12*, 17376; c) L. Xue, Q. H. Zhang, X. H. Zhu, L. Gu, J. L. Yue, Q. Y. Xia, T. Xing, T. T. Chen, Y. Yao, H. Xia, *Nano Energy* **2019**, *56*, 463.

[5] Z. X. Tai, C. M. Subramaniyam, S. L. Chou, L. N. Chen, H. K. Liu, S. X. Dou, *Adv. Mater.* **2017**, *29*, 1700605.

[6] Y. L. Deng, J. R. Mou, L. H. He, F. Y. Xie, Q. J. Zheng, C. G. Xu, D. M. Lin, *Dalton Trans.* **2018**, *47*, 367.

[7] a) A. Manthiram, *Nat. Commun.* **2020**, *11*, 1550; b) F. X. Wu, J. Maier, Y. Yu, *Chem. Soc. Rev.* **2020**, *49*, 1569; c) R. A. House, G. J. Rees, M. A. Perez-Osorio, J. J. Marie, E. Boivin, A. W. Robertson, A. Nag, M. Garcia-Fernandez, K. J. Zhou, P. G. Bruce, *Nat. Energy* **2020**, *5*, 777; d) P. F. Yan, J. M. Zheng, J. Liu, B. Q. Wang, X. P. Cheng, Y. F. Zhang, X. L. Sun, C. M. Wang, J. G. Zhang, *Nat. Energy* **2018**, *3*, 600; e) W. Lee, S. Muhammad, C. Sergey, H. Lee, J. Yoon, Y. M. Kang, W. S. Yoon, *Angew. Chem., Int. Ed.* **2020**, *59*, 2578; f) W. Liu, P. Oh, X. Liu, M. J. Lee, W. Cho, S. Chae, Y. Kim, J. Cho, *Angew. Chem., Int. Ed.* **2015**, *54*, 4440; g) G. G. Amatucci, J. M. Tarascon, L. C. Klein, *Solid State Ionics* **1996**, *83*, 167; h) A. Yamada, S. C. Chung, K. Hinokuma, *J. Electrochem. Soc.* **2001**, *148*, A224; i) S. Komaba, N. Kumagai, T. Sasaki, Y. Miki, *Electrochemistry* **2001**, *69*, 784; j) A. Ito, D. Li, Y. Sato, M. Arao, M. Watanabe, M. Hatano, H. Horie, Y. Ohsawa, *J. Power Sources* **2010**, *195*, 567.

[8] a) J. C. Hunter, *J. Solid State Chem.* **1981**, *39*, 142; b) K. Leung, *Chem. Mater.* **2017**, *29*, 2550.

[9] a) Y. Tesfamhret, H. Liu, Z. Chai, E. Berg, R. Younesi, *ChemElectroChem* **2021**, *8*, 1516; b) T. Aoshima, K. Okahara, C. Kiyohara, K. Shizuka, *J. Power Sources* **2001**, *97-8*, 377; c) D. Kim, S. Park, O. B. Chae, J. H. Ryu, Y.-U. Kim, R.-Z. Yin, S. M. Oh, *J. Electrochem. Soc.* **2012**, *159*, A193; d) W. Li, *J. Electrochem. Soc.* **2020**, *167*, 090514; e) H. Y. Asl, A. Manthiram, *Science* **2020**, *369*, 140.

[10] S. Sharifi-Asl, V. Yurkiv, A. Gutierrez, M. Cheng, M. Balasubramanian, F. Mashayek, J. Croy, R. Shahbazian-Yassar, *Nano Lett.* **2020**, *20*, 1208.

[11] J. Y. Li, C. Lin, M. Y. Weng, Y. Qiu, P. H. Chen, K. Yang, W. Y. Huang, Y. X. Hong, J. Li, M. J. Zhang, C. Dong, W. G. Zhao, Z. Xu, X. Wang, K. Xu, J. L. Sun, F. Pan, *Nat. Nanotechnol.* **2021**, *16*, 599.

[12] T. C. Liu, A. Dai, J. Lu, Y. F. Yuan, Y. G. Xiao, L. Yu, M. Li, J. Gim, L. Ma, J. J. Liu, C. Zhan, L. X. Li, J. X. Zheng, Y. Ren, T. P. Wu, R. Shahbazian-Yassar, J. G. Wen, F. Pan, K. Amine, *Nat. Commun.* **2019**, *10*, 4721.

[13] a) C. Xu, K. Marker, J. Lee, A. Mahadevegowda, P. J. Reeves, S. J. Day, M. F. Groh, S. P. Emge, C. Ducati, B. L. Mehdi, C. C. Tang, C. P. Grey, *Nat. Mater.* **2021**, *20*, 84; b) L. de Biasi, B. Schwarz, T. Brezesinski, P. Hartmann, J. Janek, H. Ehrenberg, *Adv. Mater.* **2019**, *31*, 1900985.

[14] a) A. Ito, D. Li, Y. Ohsawa, Y. Sato, *J. Power Sources* **2008**, *183*, 344; b) Q. Liu, T. Xie, Q. Xie, W. He, Y. Zhang, H. Zheng, X. Lu, W. Wei, B. Sa, L. Wang, D.-L. Peng, *ACS Appl. Mater. Interfaces* **2021**, *13*, 8239; c) L. Wang, T. Liu, A. Dai, V. De Andrade, Y. Ren, W. Xu, S. Lee, Q. Zhang, L. Gu, S. Wang, T. Wu, H. Jin, J. Lu, *Nat. Commun.* **2021**, *12*, 5370.

[15] T. Schwieters, M. Evertz, A. Fengler, M. Boerner, T. Dagger, Y. Stenzel, P. Harte, M. Winter, S. Nowak, *J. Power Sources* **2018**, *380*, 194.

[16] M. Evertz, J. Kasnatscheew, M. Winter, S. Nowak, *Anal. Bioanal. Chem.* **2019**, *411*, 277.

[17] S. Sharifi-Asl, J. Lu, K. Amine, R. Shahbazian-Yassar, *Adv. Energy Mater.* **2019**, *9*, 1900551.

[18] a) J. M. Bai, W. H. Sun, J. Q. Zhao, D. W. Wang, P. H. Xiao, J. Y. P. Ko, A. Huq, G. Ceder, F. Wang, *Chem. Mater.* **2020**, *32*, 9906; b) J. Q. Zhao, W. Zhang, A. Huq, S. T. Misture, B. L. Zhang, S. M. Guo, L. J.

Wu, Y. M. Zhu, Z. H. Chen, K. Amine, F. Pan, J. M. Bai, F. Wang, *Adv. Energy Mater.* **2017**, *7*, 1601266.

[19] a) T. C. Liu, J. J. Liu, L. X. Li, L. Yu, J. C. Diao, T. Zhou, S. N. Li, A. Dai, W. G. Zhao, S. Y. Xu, Y. Ren, L. G. Wang, T. P. Wu, R. Qi, Y. G. Xiao, J. X. Zheng, W. Cha, R. Harder, I. Robinson, J. G. Wen, J. Lu, F. Pan, K. Amine, *Nature* **2022**, *606*, 305; b) Z. Zhu, D. W. Yu, Y. Yang, C. Su, Y. M. Huang, Y. H. Dong, I. Waluyo, B. M. Wang, A. Hunt, X. H. Yao, J. Lee, W. J. Xue, J. Li, *Nat. Energy* **2019**, *4*, 1049.